Available online at www.sciencedirect.com
SCIENCE DIRECT
International Journal of Heat and Mass Transfer 49 (2006) 3211–3220
International Journal of HEAT and MASS TRANSFER
www.elsevier.com/locate/ijhmt

Numerical analysis of heat and mass transfer in the capillary structure of a loop heat pipe

Tarik Kaya *, John Goldak

Carleton University, Department of Mechanical and Aerospace Engineering, 1125 Colonel By Drive, Ottawa, Ont., Canada K1S 5B6

Received 24 February 2005; received in revised form 20 December 2005
Available online 31 March 2006

Abstract

The heat and mass transfer in the capillary porous structure of a loop heat pipe (LHP) is numerically studied and the LHP boiling limit is investigated. The mass, momentum and energy equations are solved numerically using the finite element method for an evaporator cross section. When a separate vapor region is formed inside the capillary structure, the shape of the free boundary is calculated by satisfying the mass and energy balance conditions at the interface. The superheat limits in the capillary structure are estimated by using the cluster nucleation theory. An explanation is provided for the robustness of LHPs to the boiling limit.

Keywords: Two-phase heat transfer; Boiling in porous media; Boiling limit; Loop heat pipes; Capillary pumped loops

1. Introduction

Two-phase capillary pumped heat transfer devices are becoming standard tools to meet the increasingly demanding thermal control problems of high-end electronics. Among these devices, loop heat pipes (LHPs) are particularly interesting because of several advantages in terms of robust operation, high heat transport capability, operability against gravity, flexible transport lines and fast diode action. As shown in Fig. 1, a typical LHP consists of an evaporator, a reservoir (usually called a compensation chamber), vapor and liquid transport lines and a condenser. The cross section of a typical evaporator is also shown in Fig. 1. The evaporator consists of a liquid-passage core, a capillary porous wick, vapor-evacuation grooves and an outer casing. In many LHPs, a secondary wick between the reservoir and the evaporator is also used to ensure that liquid remains available to the main wick at all times. Heat is applied to the outer casing of the evaporator, leading to the evaporation of the liquid inside the wick. The resulting vapor is collected in the vapor grooves and pushed through the vapor transport line towards the condenser. The meniscus formed at the surface or inside the capillary structure naturally adjusts itself to establish a capillary head that matches the total pressure drop in the LHP. The subcooled liquid from the condenser returns to the evaporator core through the reservoir, completing the cycle. Detailed descriptions of the main characteristics and working principles of the LHPs can be found in Maidanik et al. [1] and Ku [2].

In this present work, the heat and mass transfer inside the evaporator of an LHP is considered. The formulation of the problem is similar to a previous work performed by Demidov and Yatsenko [3], where the capillary structure contains a vapor region under the fin separated from the liquid region by a free boundary as shown in Fig. 2. Demidov and Yatsenko [3] have developed a numerical procedure and studied the growth of the vapor region under increasing heat loads. They also present a qualitative

* Corresponding author.
E-mail addresses: tkaya@mae.carleton.ca (T. Kaya), jgoldak@mrco2.carleton.ca (J. Goldak).

0017-9310/$ - see front matter © 2006 Elsevier Ltd. All rights reserved.
doi:10.1016/j.ijheatmasstransfer.2006.01.028

Nomenclature

c_p	specific heat at constant pressure [J kg^{-1} K^{-1}]
h_c	convection heat transfer coefficient [W m^{-2} K^{-1}]
h_i	interfacial heat transfer coefficient [W m^{-2} K^{-1}]
h_{fg}	latent heat of evaporation [J kg^{-1}]
J_{nc}	critical nucleation rate [nuclei m^{-3} s^{-1}]
k	thermal conductivity [W m^{-1} K^{-1}]
K	permeability [m^2]
L	length [m]
p	pressure [Pa]
Δp	pressure drop across wick [Pa]
Pe	Peclet number
Q_b	heat load for boiling limit [W]
q_{in}	applied heat flux [W m^{-2}]
Q_{in}	applied heat load [W]
r	radius [m]
r_p	pore radius [m]
Re	Reynolds number
t	thickness [m]
T	temperature [K]
$\mathbf{u}$	velocity vector [m s^{-1}]

Greek symbols

θ	angle [degrees]
μ	viscosity [Pa s]
ρ	density [kg m^{-3}]
φ	porosity
σ	liquid–vapor surface tension [N m^{-1}]

Subscripts

c	casing
eff	effective
g	groove
in	inlet
int	interface
l	liquid
max	maximum
n	normal component
sat	saturation
v	vapor
w	wick

analysis of the additional evaporation from the meniscus formed in the fin–wick corner when the vapor region is small without exceeding the fin surface. They report that the evaporation from this meniscus could be much higher than that from the surface of the wick and designs facilitating the formation of the meniscus would be desirable. Figus et al. [4] have also presented a numerical solution for the problem posed by Demidov and Yatsenko [3] using to a certain extent similar boundary conditions and a different method of solution. First, the solutions are obtained for a single pore-size distribution by using the Darcy model. Then, the solution method is extended to a wick with a varying pore-size distribution by using a two-dimensional pore network model. An important conclusion of this work is that the pore network model results are nearly identical to those of the Darcy model for an ordered single pore-size distribution. On the basis of this study, we consider a capillary structure with an ordered pore distribution possessing a characteristics single pore size. A similar problem has also been studied analytically by Cao and Faghri [5]. Unlike [3,4], a completely liquid-saturated wick is considered. Therefore, the interface is located at the surface of the wick. They indicate that the boiling limit inside the wick largely depends on the highest temperature under the fin. This statement needs further investigation especially when a vapor region under the fin is present. In a later study, Cao and Faghri [6] have extended their work to a three-dimensional geometry, where a two-dimensional liquid in the wick and three-dimensional vapor flow in the grooves separated by a flat interface at the wick surface is considered. A qualitative discussion of the boiling limit in a capillary structure is provided. They also compare the results of the two-dimensional model without the vapor flow in the grooves and three-dimensional model and conclude that reasonably accurate results can be obtained by a two-dimensional model especially when the vapor velocities are small for certain working fluids such as Freon-11 and ammonia. Based on these results, in our work, we consider a two-dimensional geometry to simplify the formulation of the problem. All these referenced works assume a steady-state process. Dynamic phenomena and specifically start-up is also extensively studied [7,8]. The superheat at the start-up and temperature overshoots is still not well understood. In this work, the transient regimes and start-up are not investigated.

One of the goals of the present study is a detailed investigation of the boiling limit in a capillary structure. Therefore, the completely liquid-saturated and vapor–liquid wick cases are both studied. The boiling limit in a porous structure is calculated by using the method developed by Mishkinis and Ochterbeck [9] based on the cluster nucleation theory of Kwak and Panton [10]. Our primary interest in this study is LHPs. In comparison, the previously referenced works focus primarily on capillary pumped loops (CPLs), a closely related two-phase heat transfer device to an LHP. Unlike in a CPL, the proximity of the reservoir to the evaporator in an LHP ensures that the wick is continuously supplied with liquid. However, there is no significant difference in the mathematical modeling of both devices especially because only a cross section of the evaporator is studied. The main difference here is that LHPs easily tolerate the use of metallic wicks with very small pore sizes, with a typical effective pore radius of 1 μm, resulting in larger available capillary pressure heads.

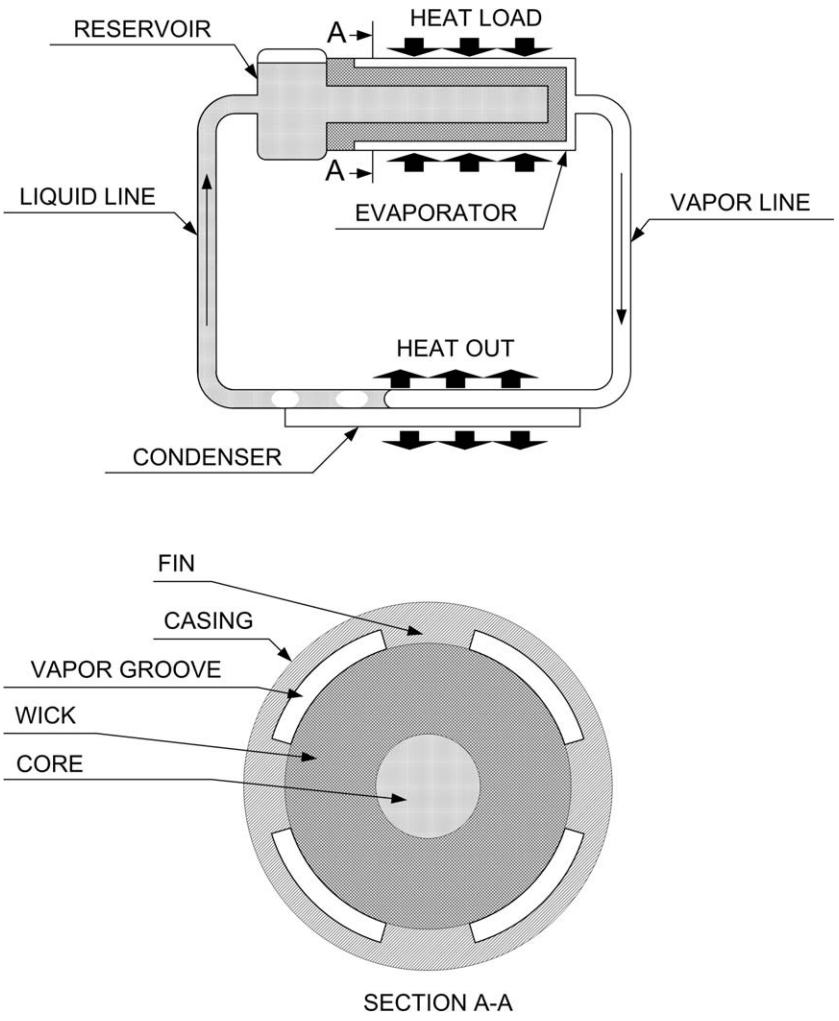

Fig. 1. Schematic of a typical LHP and cross section of the evaporator.

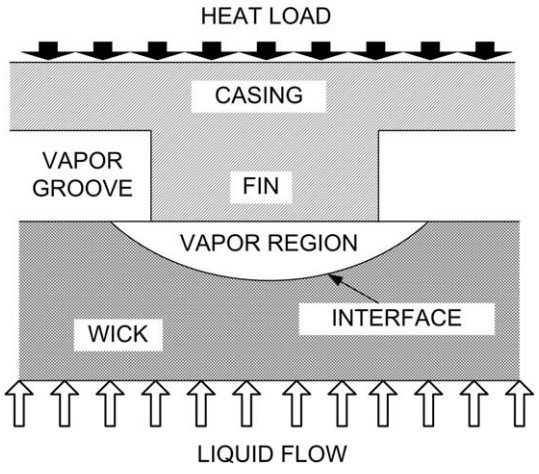

Fig. 2. Schematic of evaporation inside the evaporator.

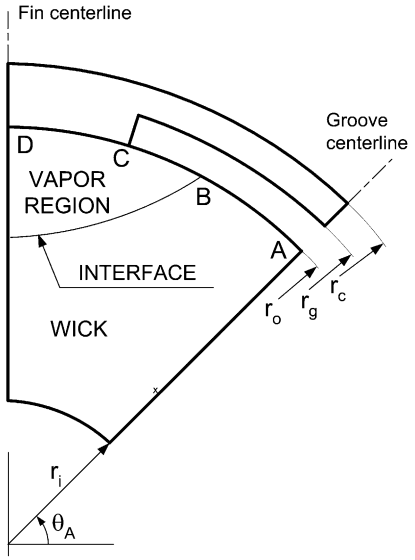

Fig. 3. Computational domain and coordinate system.

2. Mathematical formulation

A schematic of the computational model for the wick segment studied is shown in Fig. 3. Because of the symmetry, a segment of the evaporator cross section is considered, which is between the centerlines of the fin and adjacent vapor groove. The numerical solutions for this geometry

are obtained for two separate configurations. At low heat loads, the wick is entirely saturated by the liquid. At higher heat loads, the wick contains two regions divided by an interface as shown in Fig. 3: an all-vapor region in the vicinity of the fin and a liquid region in the remaining part of the wick. Heat is applied on the exterior walls of the casing and it is transferred through the fin and wick to the vapor–liquid interface. This leads to the evaporation of the liquid at the interface and thus the flow of the vapor into the grooves. For the vapor–liquid wick, the vapor formed inside the wick is pushed towards the grooves through a small region at the wick–groove border. In both of the cases, as a result of the pressure difference across the wick, the liquid from the core replaces the outflowing vapor. Under a given heat load, the system reaches the steady state and the operation is maintained as long as the heat load is applied.

The mathematical model adopted in this work is based on the following assumptions: the process is steady state; the capillary structure is homogenous and isotropic; radiative and gravitational effects are negligible; the fluid is Newtonian and has constant properties at each phase; and there is local thermal equilibrium between the porous structure and the working fluid. Many of these assumptions are similar to those made in Demidov and Yatsenko [3] and Figus et al. [4]. In addition, we also take into account convective terms in the energy (advection–diffusion) equation. The validity of the Darcy equation for the problem studied is also discussed. Under these assumptions, the governing equations for vapor and liquid phases (continuity, Darcy and energy) are as follows:

$$\nabla \cdot \mathbf{u} = 0 \tag{1}$$

$$\mathbf{u} = -\frac{K}{\mu}\nabla p \tag{2}$$

$$\rho c_p \nabla(\mathbf{u}T) = k_{\text{eff}}\nabla^2 T \tag{3}$$

It should be noted that the Darcy solver first calculates the pressure from the Laplace equation for pressure ($\nabla^2 p = 0$), which is obtained by combining Eqs. (1) and (2). The vapor flow in the groove region is not solved to simplify the problem. The boundary conditions for the liquid-saturated wick are described as follows:

At $r = r_i$

$$p = p_{\text{core}}, \quad T = T_{\text{sat}} \tag{4}$$

At $r = r_o$ and $\theta_A \leqslant \theta \leqslant \theta_C$

$$u_n = -\frac{k_{\text{eff}}}{\rho_l h_{fg}}\frac{\partial T}{\partial n}, \quad k_{\text{eff}}\frac{\partial T}{\partial n} = h_i(T - T_v) \tag{5}$$

At $r = r_o$ and $\theta_C \leqslant \theta \leqslant \theta_D$

$$\frac{\partial p}{\partial n} = 0, \quad k_c\frac{\partial T}{\partial n} = k_{\text{eff}}\frac{\partial T}{\partial n} \tag{6}$$

At $r = r_g$ and $\theta_A \leqslant \theta \leqslant \theta_C$

$$-k_c\frac{\partial T}{\partial n} = h_c(T - T_v) \tag{7}$$

At $r = r_c$

$$k_c\frac{\partial T}{\partial n} = q_{\text{in}} \tag{8}$$

At $\theta = \theta_A$ and $r_i \leqslant r \leqslant r_o$ and $r_g \leqslant r \leqslant r_c$

$$\frac{\partial p}{\partial \theta} = 0, \quad \frac{\partial T}{\partial \theta} = 0 \tag{9}$$

At $\theta = \theta_C$ and $r_o \leqslant r \leqslant r_g$

$$-k_c\frac{\partial T}{\partial n} = h_c(T - T_v) \tag{10}$$

At $\theta = \theta_D$ and $r_i \leqslant r \leqslant r_c$

$$\frac{\partial p}{\partial \theta} = 0, \quad \frac{\partial T}{\partial \theta} = 0 \tag{11}$$

In the equations above, $(\partial/\partial n)$ represents the differential operator along the normal vector to a boundary. The boundary conditions for the wick with the separate vapor and liquid regions are identical to the above equations except along the wick–groove boundary and for the vapor–liquid interface inside the wick. The following equations summarize these additional boundary conditions for the vapor–liquid wick:

At $r = r_o$ and $\theta_A \leqslant \theta \leqslant \theta_B$

$$u_n = -\frac{k_{\text{eff}}}{\rho_l h_{fg}}\frac{\partial T}{\partial n}, \quad k_{\text{eff}}\frac{\partial T}{\partial n} = h_i(T - T_v) \tag{12}$$

At $r = r_o$ and $\theta_B \leqslant \theta \leqslant \theta_C$

$$p = p_v, \quad \frac{\partial T}{\partial n} = 0 \tag{13}$$

The interface is assumed to have zero thickness. Sharp discontinuities of the material properties are maintained across the interface. The interfacial conditions are written as follows:

The mass continuity condition

$$(u_n)_v\rho_v = (u_n)_l\rho_l \tag{14}$$

The energy conservation condition

$$(k_{\text{eff}})_v\frac{\partial T_v}{\partial n} - (k_{\text{eff}})_l\frac{\partial T_l}{\partial n} = (u_n)_v\rho_v h_{fg} \tag{15}$$

For the interface temperature condition, we assume local thermal equilibrium at the interface inside the wick:

$$T_{\text{int}} = T_v = T_l \tag{16}$$

Here, we assume that the interface temperature T_{int} is given by the vapor temperature. This condition is used to locate the vapor–liquid interface as explained in the following section.

For the interface at the wick–groove border, a convective boundary condition is used, Eqs. (5) and (12). A temperature boundary condition ignoring the interfacial resistance is also possible. The interfacial heat transfer coefficient is calculated by using the relation given in Carey [11] based on the equation suggested by Silver and Simpson [12]. The heat transfer coefficient h_c between the cover plate and the vapor flow is calculated by using a correlation sug-

gested by Sleicher and Rouse [13] for fully developed flows in round ducts. It is extremely difficult to experimentally determine the heat transfer coefficient h_c and a three-dimensional model is necessary to solve the vapor flow in the grooves. A convective boundary condition is more realistic since the use of temperature boundary condition implies $h_c \to \infty$. The convective boundary condition here with a reasonable heat transfer coefficient also allows some heat flux through the groove rather than assuming the entire heat load is transferred to the wick through the fin.

3. Numerical procedure

The governing equations and associated boundary conditions described previously are solved by using the Galerkin finite element method. The computational domain under consideration is discretized with isoparametric and quadratic triangular elements.

The numerical solution sequence for the all-liquid wick is straightforward. As the entire process is driven by the liquid evaporation at the vapor–liquid front, the energy equation is first solved. The numerical solution sequence is as follows:

1. Initialize the problem by solving the energy equation assuming zero velocity inside the wick.
2. Calculate the normal component of the outflow velocity at the interface between the wick and groove from the results of the energy equation, which is then used as an outflow boundary condition for the Darcy solver.
3. Solve the Darcy equation to obtain the liquid velocity field inside the wick.
4. Solve the energy equation on the entire domain with the Darcy velocities.
5. Return to step 2 until all equations and boundary conditions are satisfied to a desired level of accuracy.

At high heat loads, when a separate vapor region develops in the wick, the numerical procedure is more complicated since the location of the interface is also an unknown of the problem. Therefore, a more involved iterative scheme is necessary. The numerical solution procedure is summarized as follows:

1. Initialize the problem by solving the Laplace equation for temperature ($\nabla^2 T = 0$) on the entire domain for a liquid-saturated wick.
2. Choose an arbitrary temperature isoline close to the fin as the initial guess for the location of the vapor–liquid interface.
3. Solve the energy equation for two separate domains: casing-vapor region and liquid region. Calculate the normal conductive heat flux at the vapor–liquid interface.
4. Solve the Darcy equation separately in the vapor and liquid regions to calculate the vapor and liquid velocities inside the wick.
5. Solve the energy equation with the Darcy velocities on the entire domain by imposing the energy conservation boundary condition at the interface.
6. Check if the temperature condition at the interface is satisfied. If it is not satisfied, the interface shape needs to be modified.
7. Return to step 3 until all equations and boundary conditions are satisfied to obtain a preset level of accuracy.

After each interface update at step 6, the solution domain needs to be remeshed. As the transient terms are not maintained in the governing equations, the numerical procedure presented is not a moving boundary technique and only the converged solutions have a physical meaning. For each solution, the static pressure drop across the interface is calculated to make sure that the difference in pressures is less than the maximum available capillary pressure in the wick ($P_v - P_l \leqslant 2\sigma/r_p$), where the normal viscous stress discontinuity and inertial forces are neglected. Thus, the momentum jump condition across the interface is satisfied as long as the maximum capillary pressure is not exceeded.

The accommodation coefficient for all the calculations is assumed to be 0.1, leading to a typical value of $h_i = 3.32 \times 10^6\ \mathrm{W\ m^{-2}\ K^{-1}}$. To test the influence of this parameter, the results are also obtained with the accommodation coefficients of 0.01 and 1. Since the resulting interfacial heat transfer coefficients are sufficiently large, the change in the maximum temperature is negligibly small, on the order of less than 0.01%. A typical value for the convection heat transfer coefficient h_c is $100\ \mathrm{W\ m^{-2}\ K^{-1}}$. The change of h_c from 100 to 50 results in an increase of less than 3% in the cover plate maximum temperature. However, the overall change in the wick temperatures is negligibly small.

4. Results and discussion

Numerical calculations are performed for the evaporator section with an outer diameter of 25.4×10^{-3} m as shown in Fig. 3. The porous wick inside the evaporator has an outer diameter of 21.9×10^{-3} and a thickness of 7.24×10^{-3} m. The wick permeability and porosity are $K = 4 \times 10^{-14}\ \mathrm{m^2}$ and $\varphi = 60\%$, respectively. The working fluid is ammonia. The LHP saturation temperature and pressure difference on both sides of the wick are calculated by using a one-dimensional mathematical model. The model is based on the steady-state energy conservation equations and the pressure drop calculations along the fluid path inside the LHP. The details of this mathematical model are presented in [14]. Fig. 4 represents the calculated saturation temperature and pressure drop values across the wick as a function of the applied power. The pressure drops and heat transfer coefficients in the two-phase regions of the LHP are calculated by using the interfacial shear model of Chen [15]. Incompressible fully developed fluid flow relations are used to calculate the pressure drop for the single phase regions.

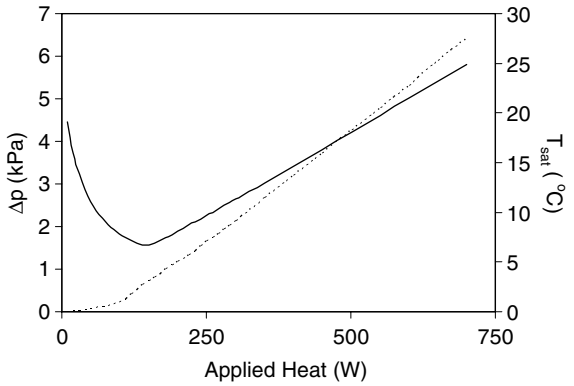

Fig. 4. Calculated pressure drop across the capillary structure and saturation temperature as a function of the applied heat (dashed line: pressure drop, solid line: saturation temperature).

Fig. 5 represents the temperature field and liquid velocity vectors when the wick is completely saturated by liquid at $Q_{in} = 100$ W. The solution is obtained by solving the mass conservation, Darcy and energy equations. At this heat load, by using the one-dimensional mathematical model, it is calculated that $T_{sat} = 7.81$ °C and $\Delta p = 247$ Pa. As the vapor flows along the grooves, it becomes superheated due to the heating from the wall. Without solving the vapor flow in the grooves using a three-dimensional model, it is not possible to calculate the vapor temperature in the grooves. Accurate experimental measurements are also difficult although a range for the vapor superheat can be deduced based on the wall-temperature measurements. In our calculations, the vapor in the grooves is assumed to be superheated by 3 °C. A similar approach is also used in Figus et al. [4]. Thus, $T_v = 10.81$ °C and other related parameters for the calculations are as follows: $P_v = 569784.8$ Pa, $P_{core} = 569537.8$ Pa, $q_{in} = 1254$ W m^{-2}, $k_c = k_w = 14.5$ W m^{-1} K^{-1}, $k_{eff} = 6.073$ W m^{-1} K^{-1}, and $h_i = 2.733 \times 10^6$ W m^{-2} K^{-1}. The thermal properties of ammonia are calculated at the saturation temperature for a given applied power using the relations in [16]. In the numerical calculations, the thermal properties are assumed constant for a given saturation temperature.

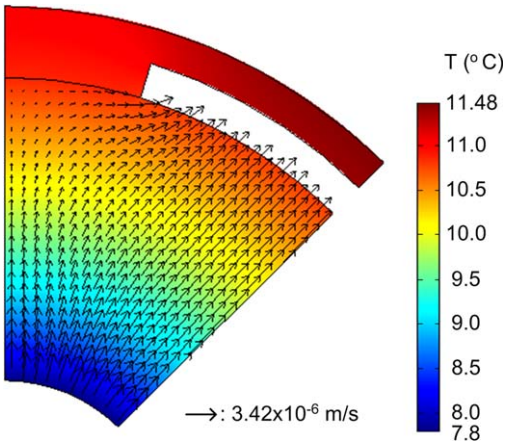

Fig. 5. Velocity vectors and temperature field at $Q_{in} = 100$ W.

It can be seen from Fig. 5 that, the working fluid evaporates at the wick interface under the applied heat load. The liquid flows from the evaporator core into the wick and turns toward the interface under the fin. The heat flux along the fin–wick interface is not constant and varies around 2000 W m^{-2}. In comparison, in the previously referenced works [3–5] with an exception in [6], an estimated constant heat flux is directly applied at the fin–wick surface and the temperature drop across the casing is ignored due to the low thermal resistance. Applying the heat at the casing allows the calculation of the temperature distribution at the casing surface. At low heat loads, the liquid velocity is relatively small as well as the corresponding Peclet number ($Pe = q_{in} L_w c_{pl} / h_{fg} k_{eff}$). For example, at $Q_{in} = 100$ W, Pe is on the order of 10^{-2}. Therefore, the contribution from the convective terms could be neglected. Therefore, in the earlier solutions [3–5], the Laplace equation for the temperature is solved instead of the full energy equation. With this assumption, the Darcy and energy equations are also decoupled, which significantly simplifies the solution algorithm. However, at higher heat loads, the convective terms need to be taken account as is done in [6]. In our study, we keep the convective terms in the governing equations and solve together the mass conservation, Darcy and energy equations as a coupled problem.

The determination of the effective thermal conductivity of the wick k_{eff} is not trivial as it depends in a complex manner on the geometry of the porous medium. The solution on Fig. 5 is obtained by assuming that there is no heat transfer between the solid porous matrix and fluid (heat transfer in parallel). This is a well-known correlation obtained by the weighted arithmetic mean of k_l and k_w ($k_{eff} = \varphi k_l + (1 - \varphi) k_w$), where φ is the wick porosity. A number of relations for the prediction of k_{eff} is proposed in the literature. To investigate the effect of k_{eff} on the results, the same problem is solved for the all-liquid wick case by using six different correlations in addition to the weighted arithmetic mean. These are weighted harmonic (heat transfer in series) and geometric means of the thermal conductivities of k_w and k_l, and other relations developed by Maxwell [17], Krupiczka [18], Zehner and Schlunder [19], and Alexander [20]. Fig. 6 represents the results obtained by using the different k_{eff} values at an arbitrarily chosen location of $\theta = 80°$. The change of slope indicates the wick and fin interface. The temperature profiles directly depend on k_{eff}. The series and parallel arrangements represent the highest and lowest conductivities, respectively. The other relations are intermediate between these two. One specific difficulty is that the correlations produce significantly different values when the thermal conductivities of the porous medium and fluid are greatly different from each other as previously studied in Nield [21]. As an example, the ratio of the thermal conductivities for the liquid and vapor regions of the wick at $T_{sat} = 7.81$ °C are $k_l/k_w = 0.0362$ and $k_v/k_w = 0.0017$, respectively. There is therefore further difficulty when both of the phases are present inside the wick. A given relation for k_{eff} will not have the same accuracy for the liquid and

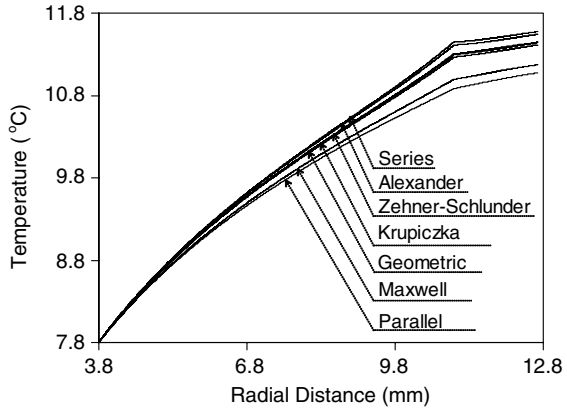

Fig. 6. Temperature profiles at $\theta = 80°$ as a function of the radial distance from the inner diameter of the wick to the outer diameter of the casing for different k_{eff} relations.

vapor regions. The effective thermal conductivity k_{eff} obtained by using different relations are given in Table 1. The results vary significantly. There is clearly a need for experimental data for an accurate determination of k_{eff}. In the lack of experimental data, we use the parallel arrangement for the rest of the numerical calculations. This is also used in several previous works [3–6]. As shown in Fig. 6, the different values of k_{eff} lead to the qualitatively similar temperature profiles. The largest temperature difference between the parallel and series solutions was within 0.5 K. The difference in temperature is small because of the low Peclet numbers. At the lower limit, as $Pe \to 0$, the energy equation reduces to the Laplace equation for temperature and the influence of k_{eff} on the temperature distribution is primarily through the flux boundary conditions. Note that the temperature at the core is imposed as a boundary condition and it has the same value for all cases.

The adequacy of using the Darcy's law for describing the flow inside the wick is also considered. For example, Cao and Faghri [6] use an expression from analogy with Navier–Stokes equation for the flow inside the porous medium, which takes into account the convective $(\mathbf{u}\cdot\nabla)\mathbf{u}/\varphi$ and viscous transport $\mu/\varphi(\nabla^2\mathbf{u})$ terms in addition to the Darcy's law. Especially at high heat flux rates, the non-Darcy flow behavior could be important. Beck [22] has showed that the inclusion of the convection term in the Darcy equation may lead to an under or over specified system of equations. Similar conclusions have also been reported in [23]. For these reasons, we do not take into account the convective terms. The maximum Reynolds number based on the effective pore diameter of the wick of 2.4 μm is on the order of 10^{-2}, which occurs in the vapor region near the fin edge. Therefore, the quadratic inertia terms are negligible in both the vapor and liquid regions. A comparison of the results obtained from Darcy and Brinkman equations for the all-liquid wick case showed that contribution from the Brinkman terms can also be safely neglected. As a result, the non-Darcy flow effects could be ignored without penalty.

Table 1
The effective thermal conductivity values for the liquid and vapor regions computed from different correlations

Relation	k_{l} (W m^{-1} K^{-1})	k_{v} (W m^{-1} K^{-1})
Harmonic mean (series arrangement)	0.849	0.040
Alexandre [20]	1.054	0.093
Zehner and Schlunder [19]	1.684	0.148
Krupiczka [18]	1.756	0.152
Geometric mean	1.967	0.309
Maxwell [17]	4.845	4.450
Arithmetic mean (parallel arrangement)	6.073	5.774

At sufficiently high heat flux values, it is expected that the nucleation will start at the microscopic cavities at the fin–wick interface. The boiling can initiate at small superheat values as a result of trapped gas in these cavities. The vapor bubbles formed at the fin–wick interface unite and lead to the formation of a vapor–liquid interface inside the wick as originally suggested by Demidov and Yatsenko [3]. With increasing heat flux, the vapor–liquid interface recedes further into the wick because of the increased evaporation and insufficient supply of the returning subcooled liquid. Thus, the vapor zone under the fin continues to grow in size and starts connecting with the vapor grooves. For a given heat load, there exists a steady-state solution for which the heat transferred to the wick from the fin surface is balanced by the convective heat output to the vapor–groove interface where the evaporation takes place. As the applied heat load is increased, the vapor region under the fin grows. For sufficiently large applied heat load, no converged solution is possible unless the removal of vapor from the interface inside the wick is allowed from the wick–groove interface.

For the transition from the all-liquid wick to the vapor–liquid wick, a boiling incipient superheat value is assumed. It is difficult to predict the incipient superheat, which depends on several parameters in a complex manner. In our calculations, when the liquid temperature under the fin is 4 °C higher than T_{sat}, it is assumed that a vapor region will form under the fin. Then, a new solution is obtained by using the numerical procedure outlined for the vapor–liquid wick. These results provide a reference base for the boiling analysis of the LHP using nuclear cluster theory, which will be addressed later in the paper. Fig. 7 represents the results obtained at a heat load of $Q_{\text{in}} = 300$ W. The LHP saturation temperature and pressure drop is $T_{\text{sat}} = 11.03$ °C and $\Delta p = 2181$ Pa, respectively. It should be noted that the one-dimensional model does not take into account the presence of a vapor region inside the wick. The change on the wick effective thermal conductivity in the presence of vapor zone needs to be estimated to improve the calculations of the boundary conditions from the one-dimensional model. An iterative procedure between the one- and two-dimensional models could be more representative. However, this would be computationally intensive and no significant change in the overall results is expected. Other required numerical values

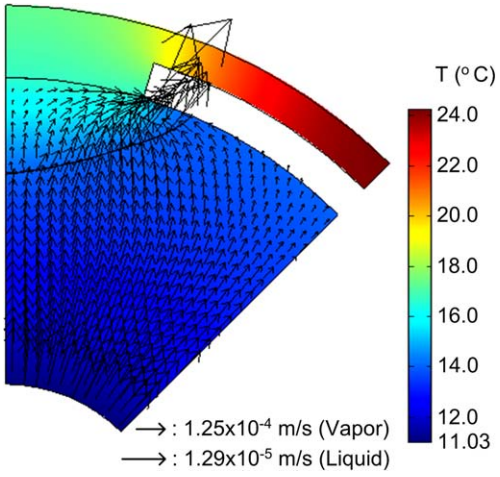

Fig. 7. Velocity vectors and temperature field at $Q_{in} = 300$ W.

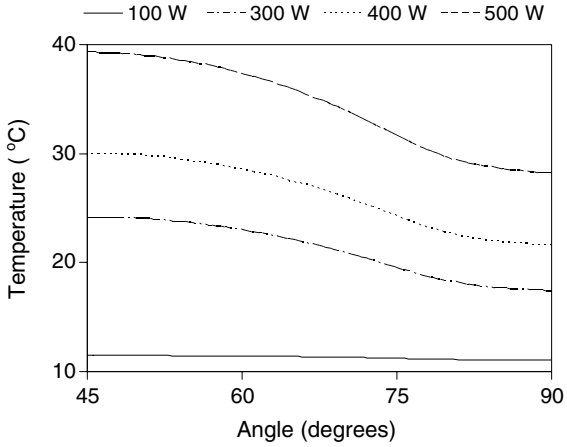

Fig. 8. Temperature profiles on the outer surface of the casing as a function of θ from the groove centerline to the fin centerline for different heat loads.

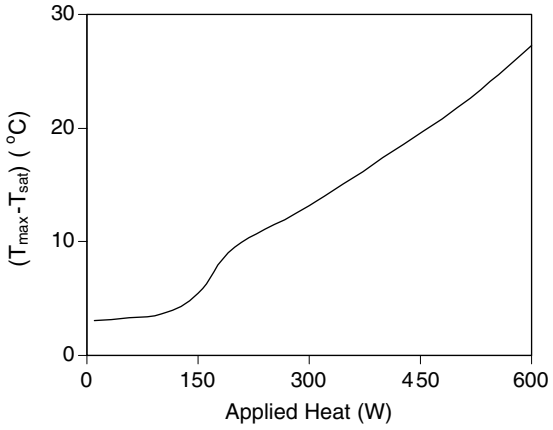

Fig. 9. Difference between the maximum temperature on the outer surface of the casing and saturation temperature as a function of the applied heat.

are calculated in the same way as previously explained for the liquid-saturated wick. Because of the large density difference between the liquid and vapor phases, the velocity for each phase is significantly different. In plotting the results, different scale factors are used for each phase as shown in Fig. 7. The highest velocities occur at the small section of the wick–groove border, which is the only outflow boundary for the vapor generated at the interface inside the wick. The applied heat is carried to the vapor–liquid interface mainly by conduction since the convection inside the vapor zone is weak and decreases with the growing size of the vapor region. The surface evaporation on the wick–groove border of the liquid-saturated section is reduced in comparison to the solution obtained with the all-liquid wick. This is due to the fact that the applied heat directly flows to the most active region of the evaporation, which is now at the vapor–liquid interface inside the wick.

As the applied heat load is increased, the vapor–liquid front inside the wick continues moving away from the fin and the size of the vapor region enlarges. Fig. 8 compares the temperature profiles on the outer surface of the casing for four different heat loads. In each case, not surprisingly, the maximum temperature is reached at the mid-point on the casing outer surface at $\theta = 45°$. The maximum temperature increases with the applied heat load as expected. The variation of $(T_{max} - T_{sat})$ as a function of the applied heat flux is shown in Fig. 9. The temperature difference increases with the heat load. At low heat loads, the temperature difference is small when the wick is completely liquid filled. The first change in slope is due to the initiation of the vapor region under the fin and the second change in slope occurs when the vapor region extends towards the groove past the fin corner region. The results presented in Fig. 9 are in good agreement with the results of the pore network model reported in [4].

The above calculations assume that the nucleation is initiated by vapor embryo trapped in the microcavities at the fin–wick interface. As a result, the anticipated incipience superheats are small, on the order of 1–4 °C. The boiling in the wick can be delayed to higher superheats by improving the contact between the fin and wick and purifying the working fluid to the greatest extent possible. In microchannels, the superheat limit can be at the same order of magnitude as that for homogenous nucleation for a pure liquid [9]. According to Zhang et al. [24], this superheat limit is the sufficient and necessary condition for the phase change in microchannels. Zhang et al. [24] also explain that the rate of phase change in microchannels is very rapid on the order of milliseconds, resulting in explosive or flash-like evaporation. This phenomena is not observed for macrochannels (several hundred microns and higher), where the rate of phase change is on the order of seconds. Without referring to flash-like evaporation, Cao and Faghri [6] have previously described that at high heat fluxes, the bubbles could be expulsed at such high pressures that they may destroy the capillary meniscus, leading to a boiling limit. This is considered as a heat transfer limit since the wick dry-out is associated with the nucleate boiling in the wick. To investigate such an explosive nucleation scenario, the superheat limit in a porous structure needs to be estimated.

Mishkinis and Ochterbeck [9] state that the classical heat-pipe boiling limitation theory is not appropriate for the capillary wicks used in LHPs and CPLs with pore sizes at the same order of the nucleation site. Instead, they apply the Kwak and Panton [10] cluster nucleation theory to two-phase capillary pumped heat transfer devices. In this study, we follow the method proposed in [9]. The porous wick is modeled as a collection of the microchannels with a diameter equal to the pore size. The critical nucleation rate J_{nc} is calculated from the wick dry-out limit condition. According to this criterion, the approximate completion time required for phase change is equal to the time required to replace the liquid inside the wick by the returning subcooled liquid. Then, the following equation can be used to estimate the critical nucleation rate J_{nc}:

$$J_{nc} = \frac{q_{in}}{h_{fg}\rho_l \pi (r_p t_w)^2} \tag{17}$$

Once the critical nucleation rate J_{nc} is estimated, the superheat limit can be calculated by using the cluster nucleation theory. In Zhang et al. [24], the condition for flash-like evaporation is that the completion time for phase change should be smaller than the time required for a pressure wave to travel from one wall to the opposite wall of a microchannel. This assumption leads to higher nucleation rates. However, as the superheat limit is a weak function of the nucleation rate the final results are not strongly affected by the choice of the completion time.

For a liquid-saturated wick, the maximum superheat is expected to be just under the fin. For the calculation of the boiling limit, the superheat limit is first calculated from the cluster nucleation theory. Then, the maximum temperature values under the fin are calculated for increasing heat loads by solving the conservation equations for a liquid-saturated wick. When the maximum temperature under the fin is equal to the superheat limit, a flash-like evaporation is expected for this heat load. Fig. 10 represents the calculated superheat temperature and LHP boiling limits as a function of the applied heat load based on the above assumption. Note that these are theoretical limits for an LHP with a high purity working fluid and good contact at the wick–fin interface. The calculations indicate that the LHP reaches the boiling limit at $Q_b = 395$ W as shown in Fig. 10. The experimental results obtained from this LHP demonstrate that this LHP can operate up to 700 W without any sign of dry-out. Therefore, these results seem to be in support of the existence of a vapor region after the boiling initiation under the fin, as originally suggested by Demidov and Yatsenko [3]. In this case, the vapor bubbles have an escape path through the wick–groove opening without destroying the meniscus. It is important to add that the flash-like evaporation occurs spontaneously, creating possibly strong transient effects. However, the sustained operation of the LHP seems to indicate that this dynamic phenomenon does not have a detrimental effect on the operation. When the vapor region grows sufficiently large the direct contact between the fin and liquid inside the wick ceases. In such a case, the boiling initiation will most likely to occur just under the evaporating meniscus. It is in fact very difficult to reach the boiling limitation under meniscus as discussed in [9]. The vapor absolute pressure is much higher than the capillary head. The typical value of the ratio between the capillary head and vapor absolute pressure in an LHP is less than 6%. As a result, the liquid under the meniscus will stay in a metastable superheated state and no boiling will occur. It should be added that the presence of non-condensable gases can encourage the boiling through the formation of a vapor embryo. Thus, the only limitation for the LHP operation will be the available capillary head. The one-dimensional model predicts the capillary limit for this LHP at $Q_{in} = 1530$ W. In Fig. 10, the superheat and corresponding boiling heat transfer limits calculated from the equations of state are also presented. The superheat limits are obtained as an average of the van der Walls and Berthelot spinodal equations as suggested in Carey [11]. The results obtained by using the two techniques are in good agreement as shown in Fig. 10. The superheat predictions are within 4.1%. The cluster nucleation method is more accurate; however, its implementation is more involved.

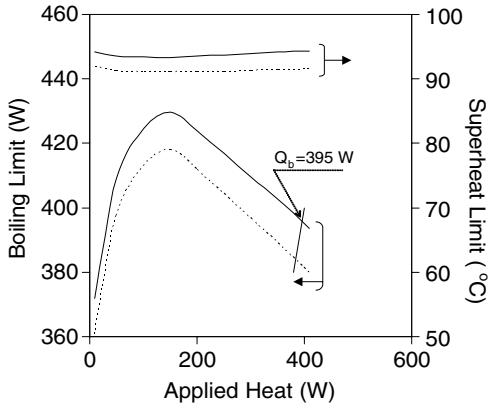

Fig. 10. Superheat and boiling limits as a function of the applied heat (solid lines: cluster nucleation theory, dashed lines: spinodal equations).

A small gap between the fin and wick to improve the efficiency of the evaporator in a CPL is suggested and analytically studied in Figus et al. [25]. The main argument is that a small gap could help venting of vapor through grooves and decrease the vapor superheating. The increase in thermal resistance due to the gap will be offset by a smaller vapor region in the wick in the presence of a gap. The estimation of the right gap size is obviously not easy. Based on the results obtained in our study, we suggest that maintaining a very good contact at the fin–wick interface will be more beneficial for the LHP operation. At low heat loads, the surface evaporation from the wick–groove interface will prevail. As it is discussed previously, at higher heat loads after the boiling incipience in the wick, the formation of a vapor region under the fin will in fact help maintaining the safe LHP operation. The influence of such a gap on boiling initiation at start-up is a separate problem and needs to be addressed as well. The experimental data obtained for a

given evaporator design during the start-up tests show that the superheat at the boiling incipience is stochastic. Dupont et al. [26] study experimentally the effect of a gap on boiling at start-up in a CPL. In this work, they show that a close fit between the fin and wick in fact decreases the superheat, where boiling starts smoothly on the wick. For a looser fit on the order of 1 mm, the boiling is more violent and it starts on the fin surface at higher superheats. This leads to a sudden pressure rise and eventually deprime. As a result, a good contact at the fin–wick interface seems to be a better design choice to reduce the incipient superheat at start-up and sustain the safe LHP operation.

5. Conclusions

The heat and mass transfer in the capillary porous structure of an LHP is investigated. The mass conservation, Darcy and energy equations are solved numerically using the finite element method. The solutions are obtained for both all-liquid and vapor–liquid wick cases. When a vapor region is present inside the wick, the interface is considered to be sharp. The mass and energy balance conditions are satisfied at the interface. The determination of the wick effective thermal conductivity k_{eff} is particularly problematic for the vapor–liquid wick since a given correlation has different accuracies for the vapor and liquid regions. However, the overall temperature distribution is not strongly affected by the choice of correlation to predict k_{eff}. The validity of the operation with a vapor pocket venting into the grooves at high heat fluxes is studied. The superheat limits in a porous structure are calculated by using the cluster nucleation theory to determine the boiling limit as a result of explosive evaporation. The experimental results indicate that at the heat loads predicted for explosive evaporation, the LHP does not experience wick dryout. At high heat loads, when the liquid contact with the fin comes to an end because of the enlarged vapor region, the boiling initiation under the evaporating meniscus is very unlikely. To increase the heat transfer limit for boiling, it is desirable to maintain a very good contact at the fin–wick interface along with the elimination of the noncondensable gases. The present work offers a numerical investigation in the explanation of the robustness of the LHP operation.

Acknowledgement

The support from Natural Sciences and Engineering Research Council of Canada under Discovery Grants Program (Grant No: RGP 261208) is appreciated.

References

[1] Y.F. Maidanik, Y.F. Fershtater, N.N. Solodovnik, Design and investigation of regulation of loop heat pipes for terrestrial and space applications, SAE Paper 941407, 1994.
[2] J. Ku, Operational characteristics of loop heat pipes, SAE Paper 1999-01-2007, 1999.
[3] A.S. Demidov, E.S. Yatsenko, Investigation of heat and mass transfer in the evaporation zone of a heat pipe operating by the 'inverted meniscus' principle, Int. J. Heat Mass Transfer 37 (14) (1994) 2155–2163.
[4] C. Figus, Y. Le Bray, S. Bories, M. Prat, Heat and mass transfer with phase change in a porous structure partially heated: continuum model and pore network simulations, Int. J. Heat Mass Transfer 42 (1999) 2557–2569.
[5] Y. Cao, A. Faghri, Analytical solutions of flow and heat transfer in a porous structure with partial heating and evaporation on the upper surface, Int. J. Heat Mass Transfer 37 (10) (1994) 1525–1533.
[6] Y. Cao, A. Faghri, Conjugate analysis of a flat-plate type evaporator for capillary pumped loops with three-dimensional vapor flow in the groove, Int. J. Heat Mass Transfer 37 (3) (1994) 401–409.
[7] T. Hoang, J. Ku, Theory of hydrodynamic stability for capillary pumped loopsNational Heat Transfer Conference, vol. 307, ASME, 1995, pp. 33–40.
[8] E. Pouzet, J.L. Joly, V. Platel, J.Y. Grandpeix, C. Butto, Dynamic response of a capillary pumped loop subjected to various heat load transients, Int. J. Heat Mass Transfer 47 (2004) 2293–2316.
[9] D. Mishkinis, J.M. Ochterbeck, Homogeneous nucleation and the heat-pipe boiling limitation, J. Eng. Phys. Thermophys. 76 (4) (2003) 813–818.
[10] H.Y. Kwak, R.L. Panton, Tensile strength of simple liquids predicted by a model of molecular interactions, J. Phys. D: Appl. Phys. 18 (1985) 647–659.
[11] V.P. Carey, Liquid–Vapor Phase-Change Phenomena, first ed., Taylor & Francis, 1992, pp. 112–120 and 150–155.
[12] R.S. Silver, H.C. Simpson, The condensation of superheated steam, in: Proceedings of a Conference Held at the National Engineering Laboratory, Glasgow, Scotland, 1961.
[13] C.A. Sleicher, M.W. Rouse, A convenient correlation for heat transfer to constant and variable property fluids in turbulent pipe flow, Int. J. Heat Mass Transfer 18 (1975) 677–683.
[14] T. Kaya, T. Hoang, Mathematical modeling of loop heat pipes and experimental validation, J. Thermophys. Heat Transfer 13 (3) (1999) 314–320.
[15] M.G. Izenson, C.J. Crowley, Design of condensing radiators for spacecraft thermal management, AIAA Paper A92-47847, 1992.
[16] P.J. Brennan, E.J. Kroliczek, Heat Pipe Design Handbook, NASA NAS5-32406, Maryland, 1979, pp. 62–67.
[17] A. Faghri, Heat Pipe Science and Technology, first ed., Taylor & Francis, 1995.
[18] R. Krupiczka, Analysis of thermal conductivity in granular materials, Int. Chem. Eng. 7 (122) (1967).
[19] P. Zehner, E.U. Schlunder, Thermal conductivity of granular materials at moderate temperature (in German), Chem. Ing. Tech. 42 (933) (1970).
[20] G.P. Peterson, L.S. Fletcher, Effective thermal conductivity of sintered heat pipe wicks, J. Thermophys. Heat Transfer 1 (4) (1987) 343–347.
[21] D.A. Nield, Estimation of the stagnant thermal conductivity of saturated porous media, Int. J. Heat Mass Transfer 34 (6) (1991) 1575–1576.
[22] J.L. Beck, Convection in a box of porous material saturated with fluid, Phys. Fluids 13 (8) (1972) 1377–1383.
[23] D.A. Nield, A. Bejan, Convection in Porous Media, second ed., Springer, New York, 1999.
[24] J.T. Zhang, X.F. Peng, G.P. Peterson, Analysis of phase change mechanisms in microchannels using cluster nucleation theory, Microscale Thermophys. Eng. 4 (3) (2000) 177–188.
[25] C. Figus, S. Bories, M. Prat, Investigation and analysis of a porous evaporator for a capillary pumped loop, in: Proceedings of the Engineering Systems and Design and Analysis Conference, ASME, 1996, pp. 99–106.
[26] V. Dupont, J.L. Joly, M. Miscevic, V. Platel, Capillary pumped loop startup: effects of the wick fit on boiling incipience, J. Thermophys. Heat Transfer 17 (2) (2003) 138–144.